Neuron
NeuroResource

Multipoint-Emitting Optical Fibers for Spatially Addressable In Vivo Optogenetics

Ferruccio Pisanello,[1,2,*] Leonardo Sileo,[1,3] Ian A. Oldenburg,[5] Marco Pisanello,[1,3] Luigi Martiradonna,[1] John A. Assad,[2,4] Bernardo L. Sabatini,[5] and Massimo De Vittorio[1,3]
[1]Istituto Italiano di Tecnologia (IIT), Center for Bio-Molecular Nanotechnologies, Via Barsanti sn, 73010 Arnesano (Lecce), Italy
[2]Center for Neuroscience and Cognitive Systems@UniTn, Istituto Italiano di Tecnologia. corso Bettini 31, 38068 Rovereto (TN), Italy
[3]Dipartimento di Ingegneria dell'Innovazione, Università del Salento, Istituto Nanoscienze-CNR, NNL-National Nanotechnology Laboratory, via per Monteroni, 73100 Lecce, Italy
[4]Department of Neurobiology, Harvard Medical School, Boston, MA 02115, USA
[5]Department of Neurobiology, Howard Hughes Medical Institute, Harvard Medical School, Boston, MA 02115, USA
*Correspondence: ferruccio.pisanello@iit.it
http://dx.doi.org/10.1016/j.neuron.2014.04.041

SUMMARY

Optical stimulation and silencing of neural activity is a powerful technique for elucidating the structure and function of neural circuitry. In most in vivo optogenetic experiments, light is delivered into the brain through a single optical fiber. However, this approach limits illumination to a fixed volume of the brain. Here a focused ion beam is used to pattern multiple light windows on a tapered optical fiber. We show that such fibers allow selective and dynamic illumination of different brain regions along the taper. Site selection is achieved by a simple coupling strategy at the fiber input, and the use of a single tapered waveguide minimizes the implant invasiveness. We demonstrate the effectiveness of this approach for multipoint optical stimulation in the mammalian brain in vivo by coupling the fiber to a microelectrode array and performing simultaneous extracellular recording and stimulation at multiple sites in the mouse striatum and cerebral cortex.

INTRODUCTION

The use of microbial opsins for optical stimulation and silencing of neuronal activity (optogenetics) facilitates understanding neural circuits and linking the activity of circuit elements to behavior (Alivisatos et al., 2013; Andrasfalvy et al., 2010; Boyden et al., 2005; Han and Boyden, 2007; Liu et al., 2012; Papagiakoumou et al., 2010; Prakash et al., 2012; Rickgauer and Tank, 2009; Zhang et al., 2007). Optogenetics has in turn created a demand for optical devices that target delivery of light to subregions of the living brain. Current spatially selective light-delivery devices for optogenetics are based on solid-state photonic waveguide array or integrated semiconductor light-emitting diodes (LEDs), each exciting a specific spot in the brain by exploiting the spatial distribution of multiple light emitters. This control has been achieved by means of several technological approaches, including amplitude or phase modulation (Anselmi et al., 2011; Grossman et al., 2010), glass-sharpened optrodes (Abaya et al., 2012a, 2012b), arrayed optical fibers (Royer et al., 2010; Stark et al., 2012), multiwaveguide fabrication on a single substrate (Zorzos et al., 2010), endoscopic fiber bundles (Hayashi et al., 2012), LED-coupled tapered fiber arrays (Stark et al., 2012), and wireless micrometer-sized LEDs on flexible shafts (Kim et al., 2013). Recently, implantable three-dimensional sets of silicon oxynitride waveguides have been developed, raising the possibility of generating 3D distributed light patterns in the brain (Zorzos et al., 2012). Individual waveguides can be addressed by a matrix of micromirrors (Zorzos et al., 2012) or separately coupled to different light sources (Stark et al., 2012), allowing optical stimulation at each point with tunable wavelength and intensity.

While these methods allow spatially selective illumination, they require a complex fabrication process and/or coupling strategy at the distal end of the waveguides. Moreover, despite the wide range of proposed devices, only a few have been tested in vivo (Hayashi et al., 2012; Kim et al., 2013; Royer et al., 2010; Stark et al., 2012; Tamura et al., 2012). These devices are also quite invasive due to the large number of implanted waveguides, oversized optical components, blunt inserting edges, and potentially high temperatures generated by implanted electronics.

Here we describe the implementation of an optogenetic tool based on a *single* waveguide that, by a simple optical strategy, can selectively and dynamically illuminate multiple brain regions. The device is minimally invasive because it comprises only one thin fiber with a sharp, tapered tip. To demonstrate the effectiveness of this device in vivo, we coupled it to a linear array of microelectrodes for simultaneous multi-site extracellular recording and optical stimulation in the brain of awake mice. In a proof-of-principle experiment to validate the methodology, we find that activation of GABAergic interneurons at different depths in primary motor cortex differentially modulate subsets of cortical neurons, suggesting cell-to-cell specificity of GABAergic inhibition in the living mammalian brain.

RESULTS

A single-core optical fiber with cladding (total diameter d_0 = 125 μm; see Experimental Procedures for further details) was

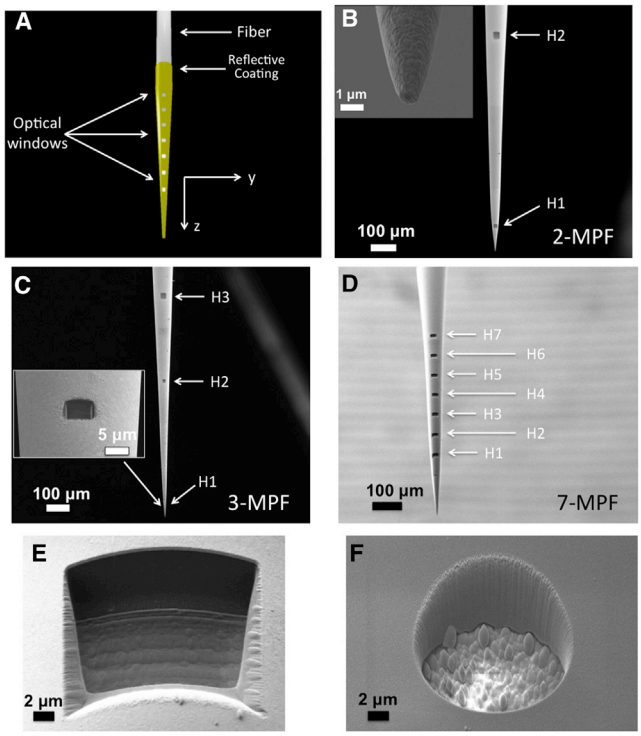

Figure 1. Multipoint-Emitting Optical Fibers

(A) Schematic representation of a seven-window multipoint-emitting optical fiber device.

(B–D) SEM micrograph of the realized devices. The inset in (B) shows the circular aperture at the taper tip. The inset in (C) shows the smallest optical window realized in the case of a three-window multipoint-emitting optical fiber.

(E and F) A square (E) and circular (F) optical window realized on the taper edge.

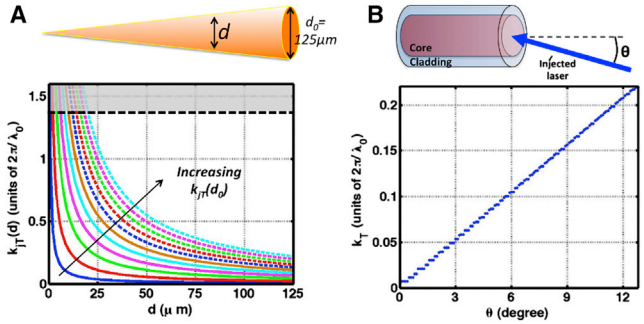

Figure 2. Modal Evolution in Multipoint-Emitting Optical Fibers

(A) $k_{jT}(d)$ evolution as a function of the taper diameter d. Each color represents a different value of $k_{jT}(d_0)$ at the taper entrance. The dashed black line represents the k_j value into the taper. For $k_{jT} > k_j$, the j-th mode becomes evanescent and lies within the gray area.

(B) k_T of the most powerful mode injected in the core/cladding section of the optical fiber, as a function of the input coupling angle θ. Details on the calculations reported in are given in Supplemental Information.

tapered and, with exception of a 200-nm-diameter circular area at the tip, was coated with gold as a reflective material (Figures 1A and 1B). The tapered shape allows selection and manipulation of propagating and evanescent modes, whereas the coating prevents leakage of light (Novotny and Hecht, 2006). Light emission is permitted at selected sites along the taper by locally removing the coating to create "windows." Illumination with a well-defined modal set at the fiber input then addresses emission to specific windows along the fiber.

The gradual taper angle (~3°–6°) and the small external diameter of the tip (~600 nm) allow smooth insertion into the brain, thereby reducing tissue damage. To obtain multiple optical windows, the reflective coating along the taper and part of the underlying material are pierced at selected points, allowing light of specific modes to escape into the surrounding environment. In the following sections we discuss three different devices, displayed in Figures 1B–1D, in which two, three, or seven optical windows were created by focused ion beam (FIB) milling (detailed geometrical parameters of each optical aperture are given in Experimental Procedures section). FIB is a particularly versatile technology for this purpose because it allows localized micromachining all along the fiber taper with a resolution better than 50 nm. Thus, optical apertures can be milled with different sizes and shapes (Figures 1E and 1F), and relatively simple optical elements, such as diffraction gratings or metallic mirrors, can be fabricated using ion- or electron-beam-induced deposition within the same system (Cheng and Steckl, 2002). We used square patterned windows for this study, but the approach can be easily extended to other types of optical elements along the taper.

Optical Properties of Multipoint-Emitting Optical Fibers in Nonscattering Medium

Each micromachined window outcouples only a fraction of the light that is guided into the fiber. The remaining radiation propagates further into the taper and undergoes a modal manipulation and selection: the transversal component of the wave vector associated to the j-th mode (k_{jT}) increases as the taper narrows (Figure 2A). As detailed in Experimental Procedures, this implies that the higher the k_{jT} value of modes at the taper entrance, the shorter the propagation length of the j-th mode into the taper. Because the lower-order modes propagate further down the taper than the higher-order modes, this allows a strategy to outcouple light from specific optical windows along the taper. The simplest way to control k_{jT} values at the taper input is to modify the input-coupling angle θ at the distal end of the fiber. The higher the input coupling angle θ, the higher the k_T of the light guided into the fiber (Figure 2B; see Supplemental Information available online for theory related to these phenomena).

In order to control the input light angle to the fiber, a λ_0 = 473 nm laser is reflected by a fixed mirror (M1) and a sliding mirror (M2), whose position defines the input coupling angle θ (Figure 3A). When the mirror M2 is in the *Home* position, the laser beam travels perpendicularly through the center of the lens, L1, which focuses the optical radiation coaxially to the optical fiber axis (θ = 0°). If the mirror is moved along the optical axis, the light is focused into the fiber coupler with a different θ.

When θ is changed, the outcoupled light intensity redistributes among the optical windows. At θ~0°, most of the light is emitted from the fiber tip (Figure S4). However, as θ is increased above ~2°, tip emission becomes negligible and most of the light is

emitted by the side apertures. Emission evolves as a function of θ, demonstrated in Figure 3 for 2-, 3-, and 7-window multipoint-emitting fibers (hereafter referred to as 2-, 3-, and 7-MPF) immersed in a fluorescein:water solution. At low θ, light is predominantly emitted by the holes closest to the tip, and in both 2- and 3-MPF nonnegligible emission takes place only at window H1 (Figures 3B1 and 3C1). Progressively increasing θ directs light emission to window H2 for the 2-MPF (Figures 3B2 and 3B3) and to H2 and then H3 for the 3-MPF (Figures 3C2 and 3C3). This allows the independent control of two or three emitting points along 700 μm, with spatially sharp emission profiles (Figures 3B4 and 3C4). In the case of the 7-MPF, the light emission is less selective among the closely spaced windows, but increasing θ still shifts the maximum of the emitted light toward the windows further from the tip, and emission from all windows defines the point of maximum intensity (Figure 3D4).

These behaviors can be explained by the modal manipulation performed by the taper on k_{jT}, whose values strongly influence the radiation efficiency of each side window (Figure S2). This is confirmed by the directionality of outcoupled light: increasing θ is accompanied by a moderate tilting of the output angle of the light beams (Figures 3B5, 3C5, and 3D5). The closer the window to the taper tip, the wider the tilting of the outcoupled beam, by virtue of the wider range of k_{jT} values between θ∼0° and θ∼12.5°.

Due to modes evanescence, the maximum outcoupling efficiency is not the same for all the side windows. Thus, the input power needed in order to emit a constant power (P_{out}) at each window varies. We determined the input power (P_{FC}) and angle (θ) required at the fiber connector to output ∼0.1 mW at the selected window while maintaining extinction ratios (the ratios of powers emitted by nonselected and selected windows) below 1:10 for 2-MPF and 1:4 for 3-MPF. In the case of a 2-MPF, this occurred for H1 with θ = 8° and P_{FC}∼2.3 mW and for H2 with θ = 12.5° and P_{FC}∼15 mW. For the 3-MPF, this required P_{FC}∼25 mW at θ = 5° (H1), P_{FC}∼22 mW at θ = 10.5° (H2), and P_{FC}∼15 mW at θ = 12.5° (H3). In contrast, in the 7-MPF the emission of all apertures contributes to the total emitting power: the input power to obtain P_{out}∼0.1 mW at 100 μm from the taper was estimated to be P_{FC}∼1.5 mW at θ = 5°, P_{FC}∼1 mW at θ = 9°, and P_{FC}∼7 mW at θ = 11.5°.

Optical Properties of Multipoint-Emitting Optical Fibers in Brain Tissue

In the brain, scattering and absorption of light by tissue determine the distribution of photons emitted by an optical fiber (Yizhar et al., 2011). To test how light emitted from the small windows on the tapered fibers behaves in scattering medium, we measured the fluorescent profiles generated by 2-, 3-, and 7-MPFs inserted into fluorescein-stained coronal mouse brain slices (Figures 4A–4C). For the 2- and 3-MPFs two main differences were observed compared to fluorescein in solution: (1) spreading of the emitted beam, as shown by the isointensity curves in Figures 4D and 4E, and (2) faster decay of light intensity due to tissue absorption (Figure 4F). Nevertheless, the active window can still be selected by changing the input-coupling angle θ for both 2- and 3-MPF (Figures 4A4 and 4B4) with only slight variations in the angle dependence compared to fluorescein in solution (Figure S8). For 7-MPF, the spread of the beam emitted by a single window results in a strongly reduced influence of θ on the selection of the illuminated brain region (Figure 4C4) with respect to fluorescein in solution.

Use of Multiple Wavelengths and Effect of Extension Fibers

MPFs also allow multiple θ and multiple wavelengths to be used at the same time, to enable simultaneous stimulation and inhibition of neural activity at two different wavelengths (Figure 5). We examined multisource illumination using the optical setup schematized in Figure 5A, where a fluorescein:TexasRed:water solution was prepared to highlight light radiation at different wavelengths. A yellow (λ_Y = 593 nm) and a blue (λ_B = 473 nm) laser were coupled into a two-window optical fiber at two different angles (θ_Y and θ_B, respectively). For θ_B = 8° and θ_Y = 12.5° the yellow light escaped predominantly from H2 by virtue of its higher input coupling angle, while the blue light was efficiently emitted at the aperture H1, as shown in Figure 5B (the blue beam excites only fluorescein, which emits at green wavelengths, while the yellow laser excites only TexasRed, emitting in the red). This suggests that the multipoint emission could be used to simultaneously elicit and inhibit neural activity in different portions of the neural tissue, through the same single waveguide. The two light sources can, moreover, emerge from the same window, as shown by the brown luminescence (combination of red and green) from H2 shown in Figure 5C (in Supplemental Information this is shown also for H1, as displayed in Figure S6B).

While all in vivo experiments reported below were carried out on head-restrained mice, the device can be easily adapted to freely behaving animals, where a short fiber stub is implanted into the moving mouse and an extension fiber is used to bring light to the stub. In order to demonstrate that the coupling at the fiber junction as well as fiber bending induced by mouse movement would not lead to significant modifications of MPFs light emission, we tested a warped 2-MPF using an extension fiber (Figure 5D). Emission properties were characterized before and after warping the fiber, to simulate animal movement. As shown in Figures 5E–5H, windows H1 and H2 could still be independently addressed by changing θ, with only slight variations of emission profiles (Figure 5I). To assess warping effects on outcoupled power (P_{out}), P_{out} was set at 0.1 mW before warping the fiber, and output power was then evaluated after warping. The rolling-unrolling experiment was performed six times. During fiber warping, at H1 we measured an average power output of 0.113 mW (SD: 0.008 mW), while at H2 we obtained 0.097 mW (SD: 0.008 mW). For comparison, the same evaluation on a standard core-cladding fiber without tapered region yielded P_{out} = 0.100 ± 0.002 mW. Warping also had very little effect on outcoupling angles: in the same experiment we found that the output angles were 18.70° ± 0.21° for H1 and 14.61° ± 0.04° for H2 for the warped fiber, compared to 18.53° for H1 and 14.62° for H2 for the nonwarped fiber. The minor effects of fiber warping on the outcoupling of light pave the way for application of MPFs to free-moving animals.

In Vivo Use of Multipoint-Emitting Optical Fibers

To test the ability to address optical excitation to different parts of the brain along the length of the fiber, we coupled 2- and

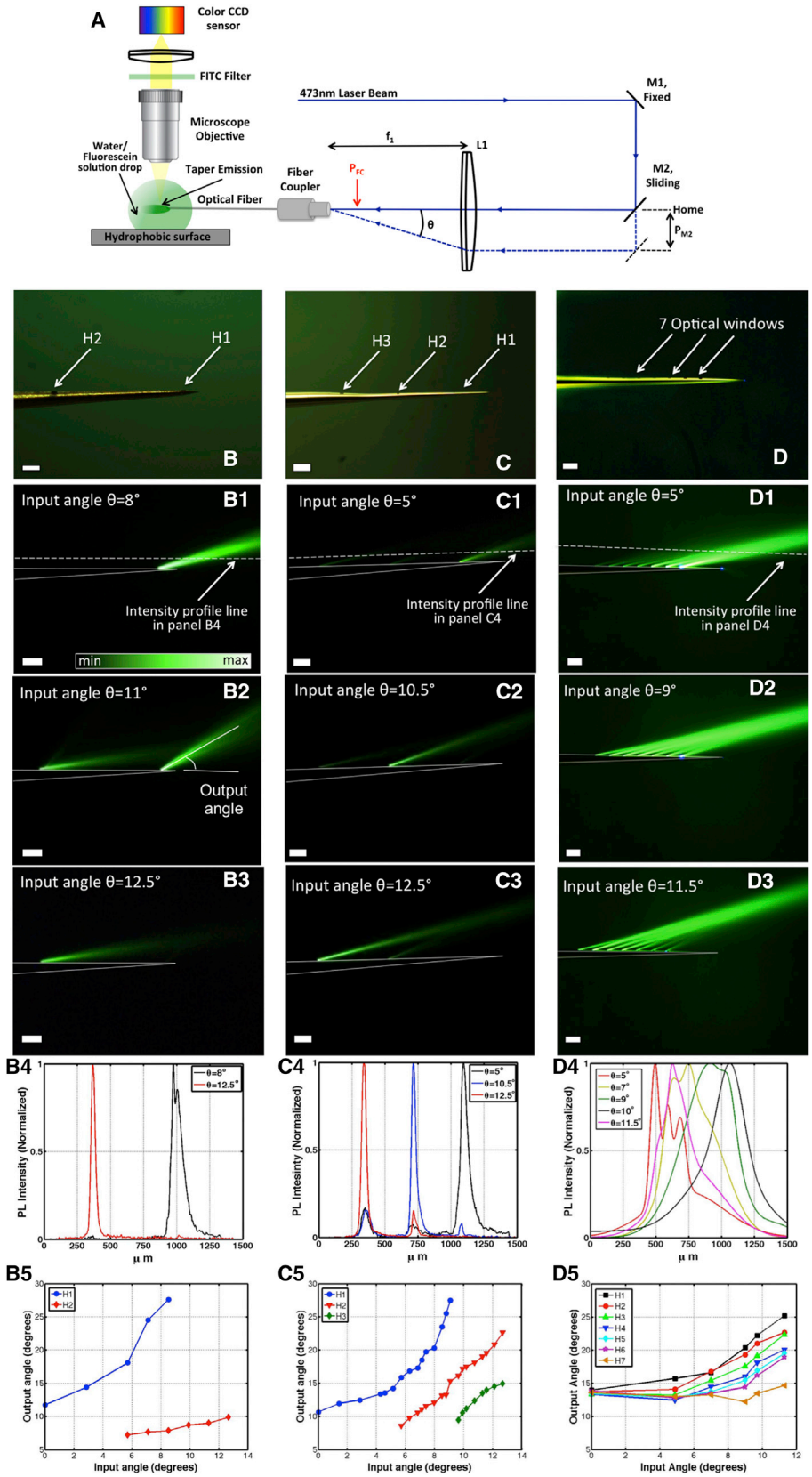

(legend on next page)

7-MPFs to a linear array of microelectrodes on a silicon shank (Neuronexus Technologies, Inc.). The microstructured optical fiber was fixed in parallel to the shank of the multielectrode (Figure 6A and Figure S9). To minimize light-induced artifacts in the recorded electrical signal (due to the Becquerel photoelectric effect) (Cardin et al., 2010; Han et al., 2009), the optical windows were oriented to illuminate the region immediately above the recording pads. To ensure that apertures were properly angled, the optrode was first tested in a phosphate-buffered saline (PBS) solution. Photoelectrical artifacts were not detectable at any laser power tested or any input coupling angle, confirming that the fiber apertures did not directly illuminate the recording pads (Figure S10). For comparison, we used the same PBS bath to test a commercial optrode, with light delivery based on a single step-index optical fiber placed just above the last recording site (model A1x16-3mm-50-413-OA16-50 from Neuronexus Technologies, Inc.). Light-induced artifacts were observed during both *OFF-ON* and *ON-OFF* light transitions at laser powers $P_{FC} \geq 33.9$ mW at the optical fiber input (Figure S10).

We tested the performance of the combined tapered fiber-multielectrode assembly with in vivo recordings in the brains of awake, head-restrained transgenic mice. P_{FC} was tuned in order to have ~0.1 mW at the selected stimulation site. To confirm selective activation of spatially separate cells, Channelrhodopsin 2 (Chr2) was expressed in striatal spiny projection neurons of the indirect pathway (iSPNs) and an optrode based on 7-MPF was used to elicit neural activity.

The tapered-fiber optrode was inserted into the mouse brain through a craniotomy, and neural activity was recorded at the multiple electrode contacts. Once the device was inserted into the striatum to a tip depth > 1,500 μm, the optrode was immobilized and left in a steady position for about 10 min to let the tissue settle. In contrast to recordings in PBS, photoelectric effects were observed at the onset light pulses in some recordings (Figure S11 and S12), possibly due to scattering of light onto the recording pads by brain tissue. Although some neuronal spikes could have been obscured by brief photoelectric effects at the light transitions, single units could be identified and clustered by principle component analysis. Evoked spike waveforms were unchanged during the laser *ON* and *OFF* periods (Figure 6B), indicating that the same unit was observed in both conditions. Because ChR2 is restricted to iSPNs, which are GABAergic, all fast excitation must be via direct ChR2 excitation. Any synaptic excitation would have to be at least disynaptic, acting via disinhibition, and would appear delayed. Thus a fast, sustained increase in neuronal firing during illumination of the GABAergic iSPNs was considered evidence of a directly activated cell.

During periods of inactivity iSPNs fire infrequently, facilitating identification of directly activated ChR2-expressing neurons. Isolated single units were observed on four recording sites, located 50 μm, 100 μm, 200 μm, and 450 μm proximal to the multielectrode tip and were selected to evaluate the performance of the device; the sites are hereafter referred as *Ch1*, *Ch2*, *Ch3*, and *Ch4*, respectively (Figure 6C). Consistent with previous reports (Kravitz et al., 2013), baseline firing rates on all channels were low (0.8 to 6.6 Hz) but could be modulated robustly by illuminating with 473 nm light. For small input coupling angles ($\theta \sim 3^\circ$), optically stimulated neuronal activity was detected at *Ch1* and *Ch2*, with firing rates increasing more than 10× at each channel ($p < 0.05$; t test on the trial-by-trial firing rates). In contrast, negligible modulation of neuronal firing was detected at the other channels (2.6× and 0.58× changes in firing rate; $p > 0.1$). With a coupling angle of ~8°, light-induced neuronal modulation was weak or absent at *Ch1* (0.7-fold increase; $p > 0.1$) and *Ch2* (3.4× increase; $p < 0.05$) but was robust at *Ch3* (11× increase; $p < 0.05$) (Figure 6C).

In contrast to the unlayered structure of the striatum, cerebral cortex provides a naturally laminated structure in which the ability to steer light through different windows permits the activation of functionally distinct cell classes. We exploited this property to ask whether the modulation of cortical neurons by local GABAergic interneurons depends on the depth of the interneuron. We used the *VGAT-ChR2* mouse line, in which ChR2 is expressed in all inhibitory interneurons. 2-MPF-based optrodes were used to activate inhibitory neurons in deep or shallow layers of mouse primary motor cortex while measuring the effects on activity of cortical neurons (Figure 6D). The light stimulus was either delivered superficially (125 μm above top recording site, < 200 μm below the pial surface) via "H2" or deep (between the 2nd and 3rd recording site, 800–1,000 μm below surface) via "H1" (Figure 6F).

Most activity was detected in deeper layers, consistent with a bias toward large pyramidal cell recordings in motor cortex. Illumination from each window was calibrated to deliver 0.1 mW of light. More than 100 pulses of light (1–10 s in duration) were delivered at the H1 and H2 windows. A unit was considered modulated by a given window if the firing rate in the first 200 ms after illumination was significantly different from a 1.5 s baseline period ($p < 0.05$, t test). Across five recordings from two animals, 61 units were recorded, 32 of which were stably isolated across the entire recording session (representative responses are displayed in Figure 6E).

Figure 3. Optical Properties of the Multipoint-Emitting Optical Fiber in fluorescein Solution

(A) Optical setup used to modify the input-coupling angle θ. A CW λ_0 = 473 nm laser beam is reflected by a fixed mirror (M1) and a sliding mirror (M2) redirects it toward lens L1. When M2 is in the *Home* position, the laser beam travels perpendicularly to L1 and through its center and is then focused onto the optical fiber. When M2 is moved by P_{M2} along the optical axis of the setup, the laser beam is still perpendicular to L1 but it is focused into the optical fiber with an angle θ. To perform optical characterization of the device, the fiber taper was immersed in a fluorescein bath and the fluorescein emission collected by an optical microscope equipped with a FITC filter and a color CCD camera.

(B–D) Light-microscope images of the 2-, 3-, and 7-window devices immersed in a drop of fluorescein:water solution with no laser coupled at its entrance. (B1–B3, C1–C3, D1–D3) Fluorescence images showing the taper emission for three different input-coupling angles. Scale bars represent 100 μm. Continuous white lines were added to highlight the taper profile. Dashed lines identify where the intensity profiles in panels B4, C4, and D4 were measured. (B4, C4, D4) Intensity profiles collected 100 μm from the fiber taper, along the white dashed lines displayed in panels B1, C1, and D1. (B5, C5, D5) Output angle as a function of the input coupling angle θ for 2-, 3-, and 7-window MPF, respectively. Output angle is defined in (B2).

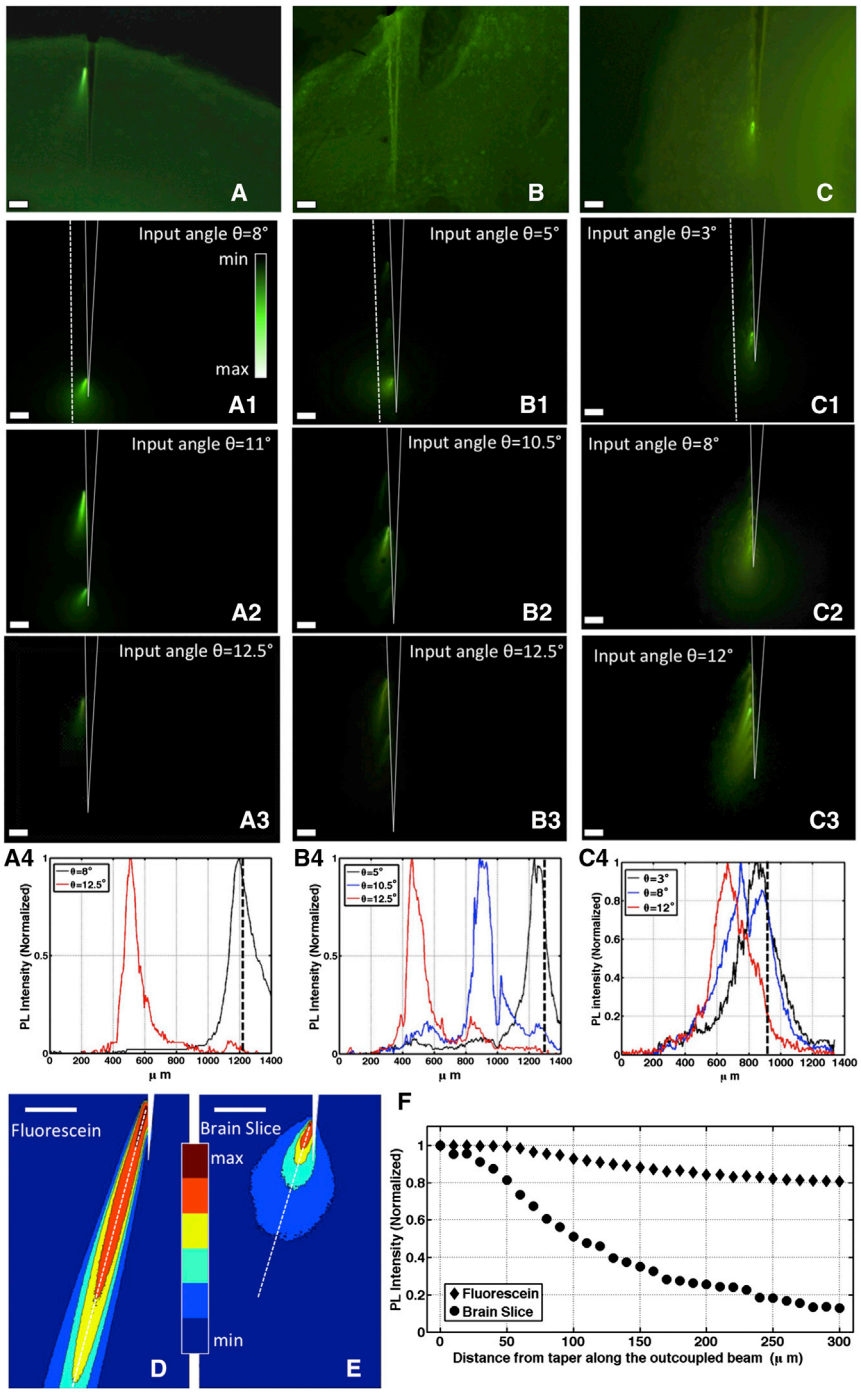

Figure 4. Optical Properties of the Multipoint-Emitting Optical Fiber in fluorescein-Stained Coronal Brain Slices

(A–C) Light-microscope images of the 2-, 3-, and 7-window devices inserted in fluorescein-stained mouse brain slices. (A1–A3, B1–B3, C1–C3) Fluorescence images showing the taper emission in fluorescein-stained mouse brain slices for three different input-coupling angles. Scale bars represent 100 μm. Continuous white lines were added to highlight the taper profile. Dashed lines identify where the intensity profiles in panels A4, B4, and C4 were measured. (A4, B4, C4) Intensity profiles collected 100 μm from the fiber taper; black dashed lines identify the position of taper tip.

(D and E) Isointensity photoluminescence curves for a single optical window emitting in fluorescein:water solution (D) and in fluorescein-stained brain slices (E). Scale bars represent 100 μm. Dashed lines identify where the intensity profiles in (F) were measured.

(F) Photoluminescence intensity decay comparison in fluorescein:water solution and brain tissue for windows H1 measured along the white dashed lines in (D) and (E), respectively.

Of the 32 stably isolated units, 13 units were not inhibited at all, and one unit was excited by H1 but not H2, presumably reflecting direct excitation of a ChR2-expressing interneuron located near H1. The remaining 18 units were inhibited, presumably through excitation of GABAergic interneurons. Five units were inhibited by light delivered through either window, and nine units were inhibited only by light delivered from H1 and not H2. Four units were inhibited by light from H2 and not H1, even though those units were located in deep cortical layers near H1, while H2 was located in superficial cortical layers (Figures 6E and 6F, and see Figure S13 for the specific changes in spike rates). Moreover, units selectively inhibited by light delivered through H1 were found on the same recording channel as those inhibited selectively by H2. Although these experiments were intended to validate the in vivo application of MPFs in layered brain regions, the data suggest that local inhibitory projections in cortex are not universally one-to-all. Rather, some neurons receive inhibitory input that is more spatially defined, such as the deep-layer units in our study that only received inhibitory input from superficial layers. While more experiments will be needed to test this hypothesis definitively, the experiment illustrates the general utility of using the multipoint-emitting fibers in parallel with electrophysiological recording to reveal aspects of local brain circuits: the experiment would not have been possible without spatially precise light stimulation of multiple locations in cortex.

DISCUSSION

Here we demonstrate a fiber-optic-based approach by which light can be delivered into the brain via multiple ports in a user-selectable manner. The advantages of this approach are that

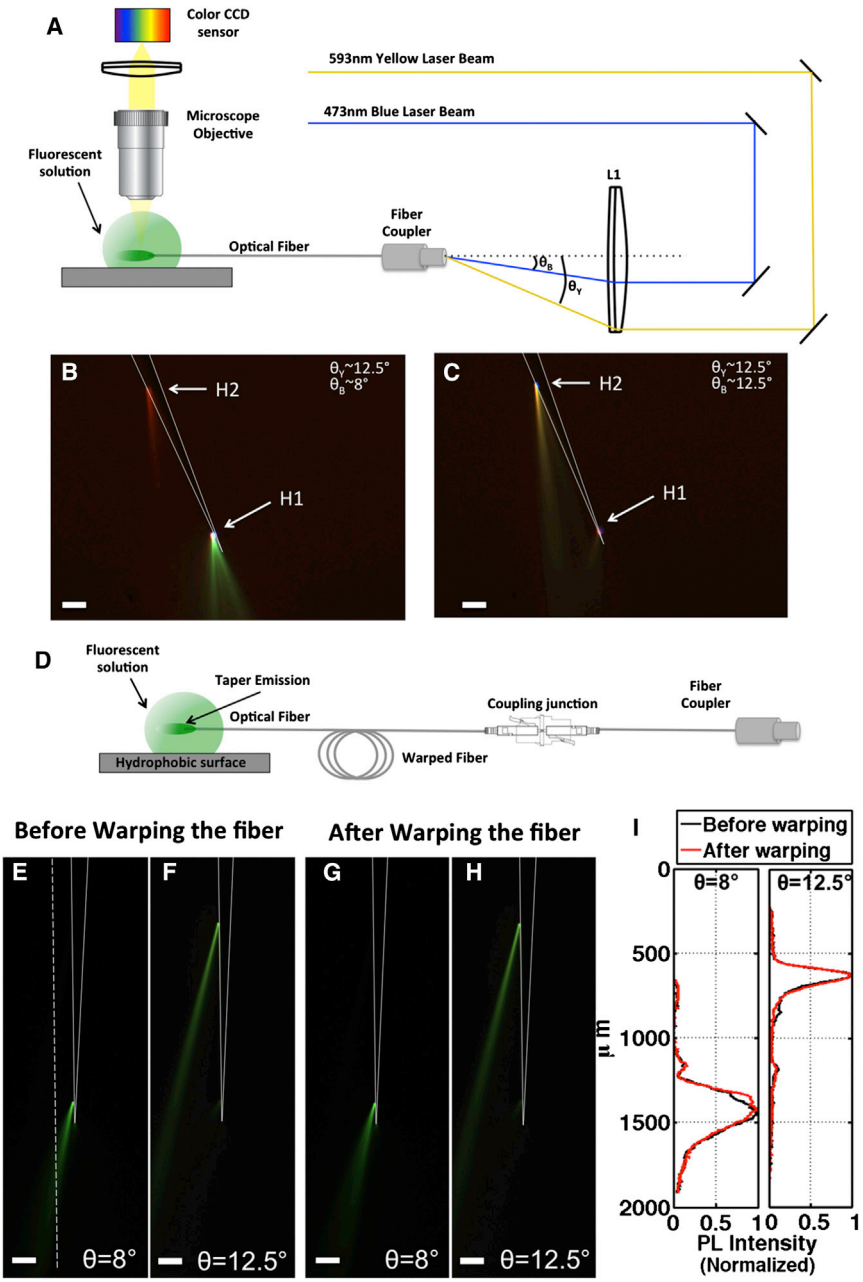

Figure 5. Two-Color Emission and Proof-of-Principle for Use of MPFs with Freely Behaving Animals

(A) Optical setup used to couple two different light beams into the optical fiber, with input coupling angles θ_B and θ_Y for blue and yellow lasers, respectively.

(B) Fluorescence image of a 2-MPF immersed in a fluorescein:TexasRed:water solution for $\theta_B \sim 8°$ and $\theta_Y \sim 12.5°$. The blue light excites only fluorescein, which emits at green wavelengths. The yellow light excites only TexasRed, emitting in the red.

(C) Fluorescence image of a 2-MPF immersed in a fluorescein:TexasRed:water solution for $\theta_B \sim 12.5°$ and $\theta_Y \sim 12.5°$. The superposition between green fluorescein luminescence and red TexasRed luminescence resulted in brown color at the CCD camera.

(D) Schematic representation of the setup used to test MPF with warped fiber and extension cords.

(E–H) Fluorescence images showing the taper emission for the configuration represented in (D) before (E and F) and after (G and H) warping the fiber, at two different θ. The fiber was rolled twice with a curvature radius of 4.5 cm. Scale bars represent 100 μm. Continuous white lines were added to highlight the taper profile. Dashed lines in (E) identify where the intensity profiles in (I) were measured.

(I) Intensity profiles before (black) and after (red) warping the fiber measured along the white dashed line in (E).

multiple regions of the brain can be stimulated via a single fiber, the light-delivery device is easily adapted for use with "optrodes," and that multiple wavelengths of light can be independently delivered via a single fiber.

In Vivo Validation

We demonstrated the utility and selectivity of the device in vivo by optogenetic activation of distinct populations of neurons via multiple optical windows on a single fiber. Within the striatum, we separately activated different populations of neurons along the length of the fiber by only changing the input angle of the ChR2-activating light to the fiber. We chose the striatum to test the spatial selectivity of the MPFs, because the baseline firing rate of striatal spiny projection neurons is low, allowing easy identification of activated ChR2-expressing neurons. Furthermore, since SPNs are inhibitory there is no possibility of intrastriatal polysynaptic excitation of non-ChR2-expressing neurons.

We also demonstrated the utility of the device for analyzing cortical microcircuits. Inhibition in cortex is critical for sensory and motor processing (Isaacson and Scanziani, 2011), yet the organization of inhibitory cortical microcircuits is unclear. There is both evidence that inhibitory neurons nonspecifically interact with all nearby pyramidal cells (Packer and Yuste, 2011) and that inhibitory neurons can have asymmetric effects (Adesnik et al., 2012). Here we recorded in vivo from neurons in primary motor cortex of an awake mouse while activating GABAergic interneurons. We found that activation of superficial versus deep interneurons can modulate different and sparse population of pyramidal neurons, consistent with high point-to-point specificity of inhibitory microcircuits. Although this preliminary result will require additional validation, it was made possible by the highly localized and spatially controlled light delivery system presented here.

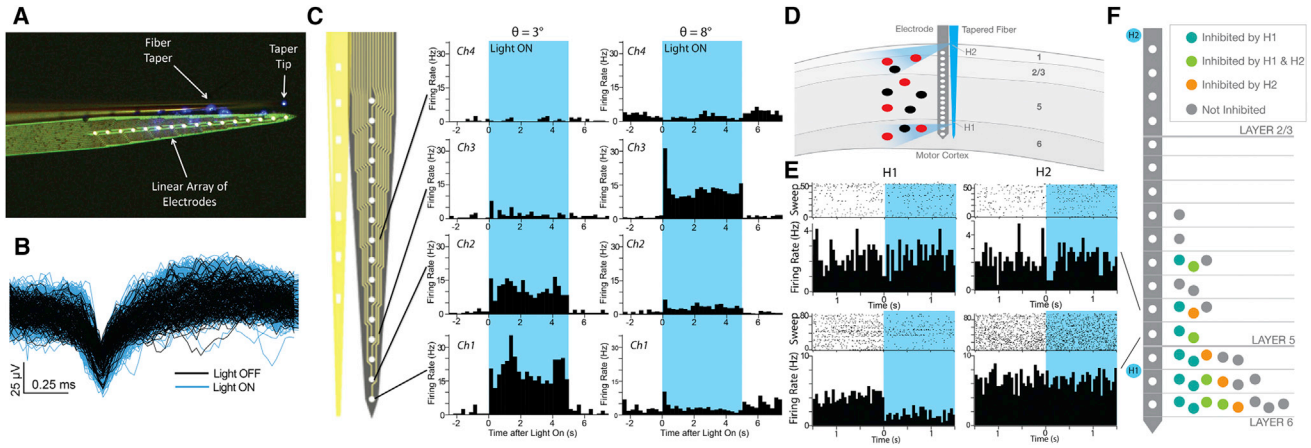

Figure 6. In Vivo Use of MPFs

(A) Light-microscope image of the structured optical fiber fixed beside a linear array of electrodes designed for extracellular recording. Optical windows on the tapered fiber were oriented to shine light in the region just above the recording pads.

(B) Overlay of sample spikes recorded at Ch2 with $\theta = 3°$. Blue curves are 1,641 spikes recorded during light ON periods, while black lines are 146 spontaneous spikes recorded during light OFF periods.

(C) In vivo recordings in striatum using a 7-MPF.

(D) Schematic representation of the in vivo experiment carried out in motor cortex.

(E) Representative spiking rate histograms recorded from single units when light was switched from OFF to H1 and from OFF to H2.

(F) Summary of the units recorded during in vivo experiments in motor cortex and their sensitivity to light outcoupled from H1 and/or H2.

Generalization of Approach

The method proposed in this paper can be customized for specific experimental needs by adjusting the size, shape, or relative placement of the windows. The key to design the multi-point-emitting optical fibers is to choose the correct size of the apertures, the appropriate fiber-taper diameter, and the correct input-coupling angles. The combination of these two last parameters defines the wave-vector transversal component k_{jT} all along the taper, allowing independent control of two or three windows along the taper length.

In summary, we developed an optogenetic device based on a tapered optical fiber that allows light to be directed to specific sites in the brain along the length of the fiber. Light escapes through a series of optical windows on the taper's edge, with the windows fabricated in a single technological step. In contrast with previously reported methods, dynamic stimulation of different brain sites was achieved by means of a single optical waveguide, thus reducing the invasiveness of the device in the brain. Site selection was achieved by a very simple optical strategy—adjusting the angle of the incident light on the input facet of the fiber. In vivo experiments, performed by coupling the optical device to a linear electrode array for extracellular signal recording, demonstrated the effectiveness of the device for switching optical activation and indirect silencing of neurons between proximal or distal recording sites in real time. The result is a powerful, versatile, and minimally invasive tool for the causal manipulation of neural circuits.

EXPERIMENTAL PROCEDURES

Optical Fiber Processing

Tapered optical fibers were purchased from Nanonics Imaging Ltd. (core diameter a = 50 μm, cladding diameter d_0 = 125 μm, core refractive index n_1 = 1.464, cladding refractive index n_2 = 1.447, numerical aperture N.A. = 0.22, taper angle between 3° and 6°, gold reflective coating thickness ~300 nm, aperture diameter at taper tip ~200 nm). Since the sharpened edge is obtained by a "heating and pulling" method, core and cladding are melted and mixed together, resulting in a homogeneous medium all along the taper. To open the optical windows, the optical fiber was inserted in a combined focused ion beam/scanning electron microscope system (FEI Helios NanoLab 600i DualBeam, equipped with the Tomahawk FIB column). For each window, a square area was scanned by the Ga^+ ion beam perpendicularly to the fiber axis (acceleration potential 30 keV, probe current 9.3 nA, dwell time 1 μs, process time up to 20 min for a 25 μm × 25 μm window and to reach a milled depth of about 6 μm). Each window was milled with sub-micrometer precision at the position targeted by SEM inspection, using the 16-bit scan/pattern generator and the integrated CAD. The scanning direction was along the positive z axis, since this produced the cleanest top sidewall of the windows, nearly free from redeposition artifacts. In the case of 2-MPFs, H1 was realized by milling an area of 15 μm × 15 μm to a depth of 4 μm at a taper diameter of 25 μm, while H2 was 25 μm × 25 μm × 6 μm (width × length × depth) at a taper diameter of 80 μm. Distance between H1 and H2 was about 700 μm. For the 3-MPF, H1 was 5 μm × 5 μm × 4 μm (taper diameter 25 μm), H2 15 μm × 15 μm × 4 μm (taper diameter 50 μm), H3 25 μm × 25 μm × 6 μm (taper diameter 85 μm). The distance between adjacent windows was ~400 μm. For the 7-MPF all windows were realized by milling an area of 25 μm × 25 μm to a depth of 6 μm and a window-to-window spacing of 100 μm.

Repeatability of the Fabrication Process

Given a certain taper angle, the process of FIB-induced milling is highly repeatable in terms of both size and optical quality of the windows, in particular because the windows milled on the cylindrical surface are two or three times smaller than the taper diameter. The distance between windows is related to the taper diameter at a given section, and thus the position of the windows has to be designed depending on the taper angle and launching parameters. Because the typical taper angle is between 3° and 6°, each multi-point-emitting optical fiber must be characterized (e.g., in fluorescein solution) before use in vivo. However, we find that ~10% of the commercially obtained tapered fibers show abrupt angle variations along the taper. These fibers are discovered by SEM inspection before FIB patterning and are

discarded. Further optimization of the tapering process, such as using a laser puller to improve the reproducibility of the taper, should reduce the number of discarded fibers.

Emitted Power Estimation

To estimate the power emitted by the optical windows, indirect measurements based on the induced fluorescence intensity were performed. The fluorescence signal of the fluorescein:water bath was calibrated using a core/cladding fiber optic without tapered region, emitting a set of known powers. FITC-filtered fluorescence images were acquired with an 8-bit CCD camera. For each known power emission, we measured the sum of the intensity values registered by the CCD over a line just outside the fiber termination, to construct a power versus intensity dependence. This procedure was repeated for different CCD acquisition parameters (gain and exposure time). The power emitted by the optical windows was then estimated through these curves. For the 2- and 3-MPFs, we recorded fluorescence images for P_{FC} = 350 μW and used the sum of the CCD counts over an imaginary line placed parallel to the taper and just outside the windows. For 7-MPFs, intensity profile was evaluated 100 μm from the taper, the same distance at which we placed the linear multielectrode array in the optrodes. Extinction ratios for 2-MPW and 3-MPF devices were computed using the estimated output powers.

Evolution of Modes in the Fiber Taper

We express the propagation vector of the *j*-th mode at the taper entrance $\boldsymbol{k}_j$ as the vectorial sum of its axial ($\boldsymbol{k}_{jA}(d_0)$) and transversal ($\boldsymbol{k}_{jT}(d_0)$) components, i.e., $\boldsymbol{k}_j = \boldsymbol{k}_{jT}(d_0) + \boldsymbol{k}_{jA}(d_0)$, with their moduli related by

$$k_{jA}(d_0) = \sqrt{k_j^2 - k_{jT}^2(d_0)},$$

and with

$$k_j = \left(\frac{2\pi n}{\lambda_0}\right),$$

constant all along the taper (*n* defines the refractive index within the taper). In general, the higher the order of the mode, the higher the transversal component of its propagation vector, i.e., $k_{jT}(d_0) \leq k_{(j+1)T}(d_0)$. All the modes excited at the distal end of the fiber propagate up to the tapered section, where their behavior is strongly modified. The transversal component of the propagation vector of the *j*-th mode is a function of the taper diameter *d*:

$$k_{jT}(d) = k_{jT}(d_0)\frac{d_0}{d},$$

where d_0 = 125 μm is the fiber diameter at the taper entrance, so that the narrower the taper, the higher the k_{jT}(d) value. For *d* small enough to have $k_{jT}(d) > k_j$, $k_{jA}(d) = \sqrt{k_j^2 - k_{jT}^2(d)}$ becomes imaginary and the *j*-th mode thus becomes evanescent. This behavior is graphically described in Figure 2A: the dashed black line represents k_j, whereas the other curves represent the evolution of $k_{jT}(d)$ for different $k_{jT}(d_0)$. The higher the propagation-vector transversal component at the taper entrance $k_{jT}(d_0)$, the higher the diameter at which $k_{jT}(d)$ overtakes k_j, thus implying evanescence of the modes in sections closer to the taper entrance. It is worth noting that modal functions as well as k_{jT} are influenced only by the shape and size of the waveguide in a particular section, while the propagation direction (forward and backward) has no influence on that parameter (Snyder and Love, 1983).

Tuning of the Input-Coupling Angle

The optical setup used to modulate the input-coupling angle is shown in Figure 3A, with additional details given in Figure S3. By sliding the mirror M2 along the optical path by P_{M2}, the input-coupling angle θ is modified, as θ = atan($|P_{M2}|/f_1$). Because the diameter of L1 is 50.8 mm, the maximum θ achievable is $\theta_{max} \sim 14^\circ$, well above the limit given by the optical fiber numerical aperture ($\alpha_{max} = 12.7^\circ$). The beam waist at L1, hereafter referred to as W_{L1}, defines instead the angular aperture of the focalized beam, as φ = atan[(W_{L1}-W_C)/f_1)], where W_C is the waist of the focused beam at the fiber entrance. In our case we found φ∼0.4°.

To examine the radiation from the optical windows, the fiber taper was immersed into a fluorescein bath (in water). Fluorescein emission excited by the aperture on the taper's edge was detected by a Zeiss microscope equipped with a FITC filter, and imaged by a CCD camera.

For experiments on brain slices, brain tissue was fixed with 4% paraformaldehyde and immersed in a fluorescein bath in PBS for one day. The fluorescent tissue was placed on a microscope coverslip, the tapered optical fiber was inserted by a micromanipulator, and optical analysis was performed following the same procedures as in the fluorescein-bath experiments.

Animal Procedures

All animal procedures were approved by the Institutional Animal Care and Use Committee at Harvard Medical School and conformed to National Institutes of Health Guidelines. Custom-made titanium head plates were surgically implanted on the skull of adult C57BL/6 mice expressing either cre recombinase in the indirect pathway spiny projection neurons (iSPNs), under the adenosine2A promoter (*Adora2A-cre*, GENSAT KG139), or expressing Channelrhodopsin in all inhibitory neurons (*VGAT-ChR2*, B6.Cg-Tg(Slc32a1-COP4*H134R/EYFP)8Gfng/J, Jackson Laboratory). In the same surgery, 1 μl of adeno associated virus (AAV) expressing cre-dependent ChR2 (AAV5.EF1.dflox.hChR2(H134R)-mCherry.WPRE.hGH vector from University of Pennsylvania Vector Core, AV-5-20297P) was injected into the dorsal striatum of the iSPN-Cre animal (coordinates 0.9 mm anterior 1.7 mm Lateral and 2.4 mm deep). After recovery the animal was habituated to head restraint for up to 90 min per day over the course of 3 weeks. For an unrelated task the mouse was trained to press a lever to receive a water reward. Twenty-four hours before the first recording, the injection craniotomy was reopened and enlarged (>1mm diameter) to allow acute electrical recordings from the motor cortex or striatum. Between uses the craniotomy was cleaned and covered.

Electrical Recording, Real-Time Signal Processing, and Data Analysis

Acute extracellular single-unit recordings were made on three consecutive days through a craniotomy using a Neuronexus 16-channel probe model A1x16-5mm-50-177-A16 fitted with the optic fiber. Data were filtered (300 hz to 10 khz) and acquired by either an A-M systems model 3600 extracellular amplifier (A-M Systems Inc., Sequim, WA, USA) equipped with a Cambridge Electronic Design Power1401 interface (CED, Cambridge, England) or a Plexon Inc. Omniplex system. Putative spikes were identified offline via level crossing and sorted by waveform based on principle component analysis using Offline sorter (Plexon Inc.) and Spike2 software (Cambridge Electronic Design). Waveforms clusters that were not synchronous across all channels, not time locked to other triggers, and not part of the "noise cluster" were identified as units and analyzed further. All analyzed units fulfilled the following criteria: < 2% interspike interval violation within 2 ms, and a continuous distribution of waveforms separate from the "noise cluster" in PCA space. Further analysis of waveform shape and firing rates was performed using custom scripts in IGOR Pro (wavemetrics).

SUPPLEMENTAL INFORMATION

Supplemental Information includes Supplemental Experimental Procedures and thirteen figures and can be found with this article online at http://dx.doi.org/10.1016/j.neuron.2014.04.041.

ACKNOWLEDGMENTS

This work was partially supported by the following: PON project "ITEM" and NIH grants NRSA F31–MH093026–01A1 to I.A.O and R01 NS046579 to B.L.S. We thank the Department of Neurobiology of Harvard Medical School for the use of the Neuro Imaging Core Facility, which provided fluorescent imaging service. Neuro Imaging Core Facility is supported in part by NINDS P30 #NS072030.

Accepted: April 15, 2014
Published: May 29, 2014

REFERENCES

Abaya, T.V., Blair, S., Tathireddy, P., Rieth, L., and Solzbacher, F. (2012a). A 3D glass optrode array for optical neural stimulation. Biomed. Opt. Express *3*, 3087–3104.

Abaya, T.V.F., Diwekar, M., Blair, S., Tathireddy, P., Rieth, L., Clark, G.A., and Solzbacher, F. (2012b). Characterization of a 3D optrode array for infrared neural stimulation. Biomed. Opt. Express *3*, 2200–2219.

Adesnik, H., Bruns, W., Taniguchi, H., Huang, Z.J., and Scanziani, M. (2012). A neural circuit for spatial summation in visual cortex. Nature *490*, 226–231.

Alivisatos, A.P., Andrews, A.M., Boyden, E.S., Chun, M., Church, G.M., Deisseroth, K., Donoghue, J.P., Fraser, S.E., Lippincott-Schwartz, J., Looger, L.L., et al. (2013). Nanotools for neuroscience and brain activity mapping. ACS Nano *7*, 1850–1866.

Andrasfalvy, B.K., Zemelman, B.V., Tang, J., and Vaziri, A. (2010). Two-photon single-cell optogenetic control of neuronal activity by sculpted light. Proc. Natl. Acad. Sci. USA *107*, 11981–11986.

Anselmi, F., Ventalon, C., Bègue, A., Ogden, D., and Emiliani, V. (2011). Three-dimensional imaging and photostimulation by remote-focusing and holographic light patterning. Proc. Natl. Acad. Sci. USA *108*, 19504–19509.

Boyden, E.S., Zhang, F., Bamberg, E., Nagel, G., and Deisseroth, K. (2005). Millisecond-timescale, genetically targeted optical control of neural activity. Nat. Neurosci. *8*, 1263–1268.

Cardin, J.A., Carlén, M., Meletis, K., Knoblich, U., Zhang, F., Deisseroth, K., Tsai, L.H., and Moore, C.I. (2010). Targeted optogenetic stimulation and recording of neurons in vivo using cell-type-specific expression of Channelrhodopsin-2. Nat. Protoc. *5*, 247–254.

Cheng, J., and Steckl, A. (2002). Focused ion beam fabricated micrograting for integrated optics applications. Selected Topics in Quantum Electronics. IEEE *8*, 1323–1330.

Grossman, N., Poher, V., Grubb, M.S., Kennedy, G.T., Nikolic, K., McGovern, B., Berlinguer Palmini, R., Gong, Z., Drakakis, E.M., Neil, M.A., et al. (2010). Multi-site optical excitation using ChR2 and micro-LED array. J. Neural Eng. *7*, 16004.

Han, X., and Boyden, E.S. (2007). Multiple-color optical activation, silencing, and desynchronization of neural activity, with single-spike temporal resolution. PLoS ONE *2*, e299.

Han, X., Qian, X.F., Bernstein, J.G., Zhou, H.H., Franzesi, G.T., Stern, P., Bronson, R.T., Graybiel, A.M., Desimone, R., and Boyden, E.S. (2009). Millisecond-timescale optical control of neural dynamics in the nonhuman primate brain. Neuron *62*, 191–198.

Hayashi, Y., Tagawa, Y., Yawata, S., Nakanishi, S., and Funabiki, K. (2012). Spatio-temporal control of neural activity in vivo using fluorescence micro-endoscopy. Eur. J. Neurosci. *36*, 2722–2732.

Isaacson, J.S., and Scanziani, M. (2011). How inhibition shapes cortical activity. Neuron *72*, 231–243.

Kim, T.I., McCall, J.G., Jung, Y.H., Huang, X., Siuda, E.R., Li, Y., Song, J., Song, Y.M., Pao, H.A., Kim, R.-H., et al. (2013). Injectable, cellular-scale optoelectronics with applications for wireless optogenetics. Science *340*, 211–216.

Kravitz, A.V., Owen, S.F., and Kreitzer, A.C. (2013). Optogenetic identification of striatal projection neuron subtypes during in vivo recordings. Brain Res. *1511*, 21–32.

Liu, X., Ramirez, S., Pang, P.T., Puryear, C.B., Govindarajan, A., Deisseroth, K., and Tonegawa, S. (2012). Optogenetic stimulation of a hippocampal engram activates fear memory recall. Nature *484*, 381–385.

Novotny, L., and Hecht, B. (2006). Principles of nano-optics. (Cambridge, UK: Cambridge University Press).

Packer, A.M., and Yuste, R. (2011). Dense, unspecific connectivity of neocortical parvalbumin-positive interneurons: a canonical microcircuit for inhibition? J. Neurosci. *31*, 13260–13271.

Papagiakoumou, E., Anselmi, F., Bègue, A., de Sars, V., Glückstad, J., Isacoff, E.Y., and Emiliani, V. (2010). Scanless two-photon excitation of channelrhodopsin-2. Nat. Methods *7*, 848–854.

Prakash, R., Yizhar, O., Grewe, B., Ramakrishnan, C., Wang, N., Goshen, I., Packer, A.M., Peterka, D.S., Yuste, R., Schnitzer, M.J., and Deisseroth, K. (2012). Two-photon optogenetic toolbox for fast inhibition, excitation and bistable modulation. Nat. Methods *9*, 1171–1179.

Rickgauer, J.P., and Tank, D.W. (2009). Two-photon excitation of channelrhodopsin-2 at saturation. Proc. Natl. Acad. Sci. USA *106*, 15025–15030.

Royer, S., Zemelman, B.V., Barbic, M., Losonczy, A., Buzsáki, G., and Magee, J.C. (2010). Multi-array silicon probes with integrated optical fibers: light-assisted perturbation and recording of local neural circuits in the behaving animal. Eur. J. Neurosci. *31*, 2279–2291.

Snyder, A.W., and Love, J. (1983). Optical Waveguide Theory. (London: Chapman and Hall).

Stark, E., Koos, T., and Buzsáki, G. (2012). Diode probes for spatiotemporal optical control of multiple neurons in freely moving animals. J. Neurophysiol. *108*, 349–363.

Tamura, K., Ohashi, Y., Tsubota, T., Takeuchi, D., Hirabayashi, T., Yaguchi, M., Matsuyama, M., Sekine, T., and Miyashita, Y. (2012). A glass-coated tungsten microelectrode enclosing optical fibers for optogenetic exploration in primate deep brain structures. J. Neurosci. Methods *211*, 49–57.

Yizhar, O., Fenno, L.E., Davidson, T.J., Mogri, M., and Deisseroth, K. (2011). Optogenetics in neural systems. Neuron *71*, 9–34.

Zhang, F., Wang, L.P., Brauner, M., Liewald, J.F., Kay, K., Watzke, N., Wood, P.G., Bamberg, E., Nagel, G., Gottschalk, A., and Deisseroth, K. (2007). Multimodal fast optical interrogation of neural circuitry. Nature *446*, 633–639.

Zorzos, A.N., Boyden, E.S., and Fonstad, C.G. (2010). Multiwaveguide implantable probe for light delivery to sets of distributed brain targets. Opt. Lett. *35*, 4133–4135.

Zorzos, A.N., Scholvin, J., Boyden, E.S., and Fonstad, C.G. (2012). Three-dimensional multiwaveguide probe array for light delivery to distributed brain circuits. Opt. Lett. *37*, 4841–4843.